

# Spectroscopy of an extreme [O III] emitting active galactic nucleus at $z = 3.212$ : implications for the reionization era

Mengtao Tang<sup>1</sup>,<sup>\*</sup> Daniel P. Stark,<sup>2</sup> Richard S. Ellis,<sup>1</sup> Stéphane Charlot,<sup>3</sup> Anna Feltre<sup>4</sup>,<sup>5</sup>  
Alice E. Shapley<sup>5</sup> and Ryan Endsley<sup>2</sup>

<sup>1</sup>Department of Physics and Astronomy, University College London, Gower Street, London WC1E 6BT, UK

<sup>2</sup>Steward Observatory, University of Arizona, 933 N Cherry Ave, Tucson, AZ 85721, USA

<sup>3</sup>Institut d'Astrophysique de Paris, UMR7095, CNRS, Sorbonne Université, F-75014 Paris, France

<sup>4</sup>INAF – Osservatorio di Astrofisica e Scienza dello Spazio di Bologna, Via P. Gobetti 93/3, I-40129 Bologna, Italy

<sup>5</sup>Department of Physics and Astronomy, University of California, Los Angeles, 430 Portola Plaza, Los Angeles, CA 90095, USA

Accepted 2021 November 8. Received 2021 November 1; in original form 2021 September 9

## ABSTRACT

Reionization-era galaxies often display intense nebular emission lines, both in rest-frame optical ([O III] + H $\beta$ ) and ultraviolet (UV; C III], C IV). How such strong nebular emission is powered remains unclear, with both active galactic nuclei (AGNs) and hot stars considered equally viable. The UV continuum slopes of these early systems tend to be very blue ( $\beta < -2$ ), reflecting minimal dust obscuration, young ages, and low metallicities. This contrasts with narrow-lined AGNs at  $z \sim 2-3$ , whose UV slopes are significantly redder ( $\beta > -1$ ) than typical star-forming systems in the reionization era. To investigate the properties of AGNs in the reionization era, we have conducted a search for potential examples of rare analogues with blue continua at intermediate redshift ( $z \sim 2-3$ ). Our goals are to determine whether AGNs with intense line emission and blue continua exist and thereby to establish the range of rest-frame UV and optical line ratios in this population. In this paper, we report the detection of an X-ray luminous AGN at  $z = 3.21$  (UDS-24561) with extreme [O III] + H $\beta$  line emission (equivalent width = 1300 Å) and a blue UV continuum slope ( $\beta = -2.34$ ). MMT/Binospec and Keck/MOSFIRE spectra indicate rest-frame UV line ratios consistent with AGN photoionization models and rest-frame optical lines with both a narrow component [full width at half-maximum (FWHM) = 154 km s<sup>-1</sup>] and extended broad wings (FWHM = 977 km s<sup>-1</sup>), consistent with outflowing gas. We describe how such objects can be identified in future *James Webb Space Telescope* emission line surveys in the reionization era, thereby providing a valuable census of AGN activity at  $z > 6$  and understanding their contribution to cosmic reionization.

**Key words:** galaxies: active – galaxies: evolution – galaxies: formation – galaxies: high-redshift – cosmology: observations.

## 1 INTRODUCTION

Studying the reionization of the intergalactic hydrogen is a major frontier in modern astrophysics, and provides important clues to understanding the history of cosmic structure formation (Loeb & Barkana 2001). The timeline of the reionization process has been constrained by a series of observations undertaken over the last two decades. Measurement of the optical depth to Thomson scattering of the cosmic microwave background radiation by the *Planck* team indicates a mid-point at  $z = 7.7$  (Planck Collaboration VI 2020). This is supported by a census of Ly $\alpha$  emitting galaxies at high redshift suggesting that the intergalactic medium (IGM) has a significant neutral hydrogen fraction ( $x_{\text{H I}} \sim 50$  per cent) at  $z \sim 7.5$  (see Ouchi, Ono & Shibuya 2020 for a review). Moreover, the redshift-dependent flux seen in the Ly $\alpha$  forest of quasar spectra implies a nearly fully ionized IGM and hence that the reionization process is effectively complete by  $z \simeq 6$  (e.g. Fan et al. 2006; McGreer, Mesinger & D'Odorico 2015).

However, the nature of the sources responsible for cosmic reionization is still a matter of debate. Over the last decade, thousands of star-forming galaxies (SFGs) at  $z > 6$  have been detected in deep *Hubble Space Telescope* (*HST*) imaging surveys (e.g. Bouwens et al. 2015a; Finkelstein et al. 2015; Oesch et al. 2018) and a popular view is that such sources provide the major contribution to reionization (e.g. Bouwens et al. 2015b; Robertson et al. 2015; Stanway, Eldridge & Becker 2016; Dayal & Ferrara 2018). However, if all SFGs contribute equally, (i) the ultraviolet (UV) luminosity function of  $z > 6$  galaxies must extend to intrinsically feeble systems with  $M_{\text{UV}} \simeq -13$  and (ii) the fraction of ionizing radiation that escapes into the IGM (the so-called escape fraction,  $f_{\text{esc}}$ ) must be as high as  $\simeq 20$  per cent (see Stark 2016 for a review). These requirements can be alleviated if rarer, more luminous systems make a more significant contribution, as suggested by the claimed rapid decline of the neutral fraction of the IGM over  $6 \lesssim z \lesssim 7.5$  (e.g. Naidu et al. 2020). A possible explanation for this sudden end to reionization is that many luminous sources may host active galactic nuclei (AGNs) with both harder radiation fields (e.g. Steidel et al. 2014; Stark et al. 2015; Feltre, Charlot & Gutkin 2016) and larger escape fractions ( $f_{\text{esc}} \sim 75-100$  per cent; e.g. Cristiani et al. 2016; Grazian et al. 2018).

\* E-mail: mengtao.tang@ucl.ac.uk

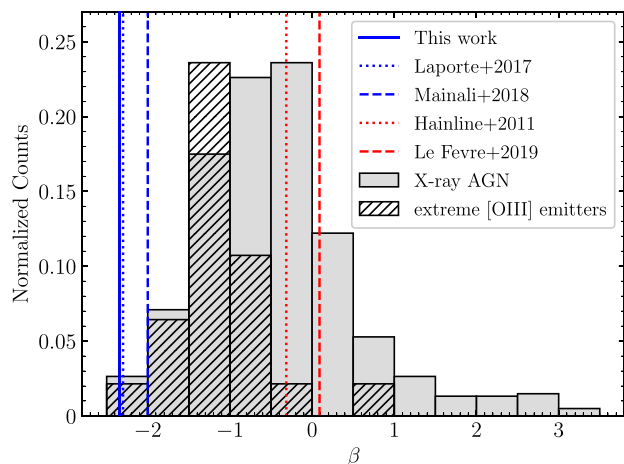


**Figure 1.** UV slope ( $\beta$ ) distribution of all the X-ray AGNs at  $z = 1.3\text{--}3.7$  in the five CANDELS fields (606 objects; grey histogram) and that of the extreme [O III] emitting AGNs (21 objects; black hatched histogram), of which the y-axis is rescaled to normalized counts. UV slopes are derived from the Barro et al. (2019) catalogues by cross-matching with *Chandra* catalogues in CANDELS fields (Xue et al. 2011, 2016; Nandra et al. 2015; Civano et al. 2016; Kocevski et al. 2018). The UV slopes of X-ray AGNs at  $z = 1.3\text{--}3.7$  are relatively red (median  $\beta = -0.5$ ), consistent with the red UV slopes found in the stacked spectra of type II AGNs at  $z \sim 2\text{--}4$  in Hainline et al. (2011) (red dotted line) and Le Fèvre et al. (2019) (red dashed line), while the extreme [O III] emitting AGNs show bluer UV slopes (median  $\beta = -1.0$ ). On the other hand, the N v emitting AGNs at  $z > 7$  (Laporte et al. 2017, blue dotted line; Mainali et al. 2018, blue dashed line) and the  $z = 3.21$  AGNs studied in this paper, UDS-24561 (blue solid line), have much bluer UV slopes of  $\beta < -2.0$ .

At present, there is only indirect evidence supporting the hypothesis of AGN activity in galaxies at  $z > 6$ . High-ionization UV emission lines (e.g. N v  $\lambda\lambda 1238, 1243$ , C IV  $\lambda\lambda 1548, 1550$ ) have been detected in a handful of star-forming galaxies (e.g. Tilvi et al. 2016; Hu et al. 2017; Laporte et al. 2017; Mainali et al. 2018; Sobral et al. 2019; Endsley et al. 2021b; Onoue et al. 2021). Although many AGNs have been found in SFGs at  $z \sim 2\text{--}4$  (e.g. Hainline et al. 2011), it seems the limited number of corresponding reionization-era systems with potential AGN signatures show very different properties. This may make it questionable to identify AGNs in  $z > 6$  systems using the predominant spectral features seen in  $z \sim 2\text{--}4$  AGNs. Specifically, SFGs in the reionization era often display rest-frame optical emission lines with extremely high equivalent widths (EWs), with an average [O III] + H  $\beta$  EW  $\simeq 700 \text{ \AA}$  at  $z \sim 7\text{--}8$  (Labbé et al. 2013; De Barros et al. 2019; Endsley et al. 2021a). Such intense lines are seldom seen in lower redshift SFGs with AGNs (e.g. Tang et al. 2019). Likewise,  $z > 6$  galaxies have very steep UV continuum slopes ( $\beta < -2.0$ ; e.g. Bouwens et al. 2012, 2014; Finkelstein et al. 2012) indicating metal-poor stellar populations with little dust. On the other hand, AGNs at  $z \sim 2\text{--}4$  present much redder UV slopes ( $\beta > -1$ , Fig. 1; e.g. Hainline et al. 2011; Le Fèvre et al. 2019), presumably because they are hosted by more massive galaxies with increased dust extinction (e.g. Hainline et al. 2012). A key question is whether these differences suggest that the nature and properties of AGNs evolve significantly between  $z \sim 2\text{--}3$  and  $z > 6$ , and that a population of blue, extreme optical line emitting galaxies harbouring AGNs are somehow more abundant in the reionization era.

The above question has motivated us to search for examples of AGN activity in  $z \simeq 1\text{--}3$  SFGs with blue UV slopes and

extreme optical line emission. To accomplish this, we exploit our large spectroscopic survey of extreme [O III] emitting galaxies at  $z = 1.3\text{--}3.7$  at rest-frame optical (Tang et al. 2019, hereafter T19) and UV wavelengths (Tang et al. 2021a, b, hereafter T21a, T21b), targeting selected systems for evidence of AGN activity using diagnostic UV and optical emission lines in the context of photoionization models (e.g. Allen et al. 2008; Feltre et al. 2016; Jaskot & Ravindranath 2016; Nakajima et al. 2018; Hirschmann et al. 2019; Plat et al. 2019). This enables us to distinguish between spectra powered by AGNs and massive stars. In this paper, we present the case of a  $z = 3.212$  AGN with extremely large EW [O III] emission with a steep UV continuum slope whose properties are thus similar to SFGs in the reionization era (e.g. Endsley et al. 2021a). Our ultimate goal is to build a statistical sample of such  $z \simeq 1\text{--}3$  AGNs that may guide future spectroscopic searches for AGN activity in the reionization era using future facilities such as the *James Webb Space Telescope* (*JWST*) or new generation of 30-m class telescopes that can target the relevant UV and optical nebular emission lines.

The organization of this paper is as follows. We describe our target selection and the spectroscopic observations in Section 2. The emission line measurements and the associated line ratio diagnostics that support evidence of AGN activity are discussed in Section 3. Finally, we discuss the implications of our results for the contribution of AGN to the reionization era in Section 4. We adopt a  $\Lambda$ -dominated, flat universe with  $\Omega_\Lambda = 0.7$ ,  $\Omega_M = 0.3$ , and  $H_0 = 70 \text{ km s}^{-1} \text{ Mpc}^{-1}$ . All magnitudes in this paper are quoted in the AB system (Oke & Gunn 1983), and all EWs are quoted in the rest frame.

## 2 OBSERVATIONS

In this work, we aim to locate and study the rest-frame UV and optical spectra of AGN with extremely large EW [O III] line emission and blue UV slopes. Our candidates will be chosen from a parent sample of extreme [O III] emitting AGNs at  $z = 1.3\text{--}3.7$ . We describe the pre-selection of targets in Section 2.1, and the spectroscopic observations in Sections 2.2–2.4.

### 2.1 Pre-selection of extreme line emitting AGNs with blue UV continuum slopes at $z = 1.3\text{--}3.7$

The first step of this study is to locate AGN candidates with extreme EW [O III] line emission and blue UV slopes for spectroscopic follow-up. In T19, we discuss the selection of a sample of extreme [O III] emitting objects at  $z = 1.3\text{--}3.7$  in the Cosmic Assembly Near-infrared Deep Extragalactic Legacy Survey (CANDELS) fields (Grogin et al. 2011; Koekemoer et al. 2011) and their near-infrared (rest-frame optical) spectra. We direct the reader to T19 for details. In brief, extreme [O III] emitters were selected to have large rest-frame [O III]  $\lambda\lambda 4959, 5007$  EWs with values  $\simeq 300\text{--}3000 \text{ \AA}$  chosen to match the range common in reionization-era sources (e.g. Endsley et al. 2021a). The [O III] EWs were inferred from *HST* grism spectra (at  $z = 1.3\text{--}2.4$ ; T19) or the *K*-band flux excess (at  $z = 3.1\text{--}3.7$ ; Tang et al., in preparation) using the 3D-*HST* catalogues (Brammer et al. 2012; Skelton et al. 2014; Momcheva et al. 2016).

To identify which are AGNs, we cross-match our  $z = 1.3\text{--}3.7$  extreme [O III] emitter sample to deep *Chandra* X-ray source catalogues in the All-Wavelength Extended Groth Strip International Survey (AEGIS; Nandra et al. 2015), the Cosmic Evolution Survey (COSMOS; Civano et al. 2016), the Great Observatories Origins Deep Survey North (GOODS-N; Xue et al. 2016) and South (GOODS-S; Xue et al. 2011), and the Ultra Deep Survey (UDS; Kocevski et al. 2018) fields. The *Chandra* X-ray data used in the five

CANDELS fields were reduced following the prescription described in Laird et al. (2009) and Nandra et al. (2015). The depths of the X-ray data are 800 ks in AEGIS, 160 ks in COSMOS, 2 Ms in GOODS-N, 4 Ms in GOODS-S, and 600 ks in UDS, resulting in hard band (2–10 keV) flux limits (over >1 per cent of the survey area) of  $2.5 \times 10^{-16}$ ,  $1.8 \times 10^{-15}$ ,  $5.9 \times 10^{-17}$ ,  $5.5 \times 10^{-17}$ , and  $6.5 \times 10^{-16}$  erg s<sup>-1</sup> cm<sup>-2</sup>, respectively. We match the coordinates of the extreme [O III] emitting objects (from the 3D-*HST* catalogues) to the X-ray source catalogues using a 1.0 arcsec search radius. There are 21 sources in our sample found to have X-ray counterparts within 1.0 arcsec.

We next examine whether the X-ray luminosities ( $L_X$ ) of the 21 sources are consistent with those of X-ray AGNs, which typically have  $L_X \gtrsim 10^{42}$  erg s<sup>-1</sup> at rest-frame 2–10 keV. The X-ray luminosities of our sources were estimated by fitting the X-ray spectra assuming a power law with index  $\Gamma = 1.7$ –1.8 for intrinsic AGN spectra (AEGIS: Buchner et al. 2015; COSMOS: Marchesi et al. 2016; GOODS-N: Xue et al. 2016; GOODS-S: Xue et al. 2011; UDS: Kocevski et al. 2018). The absorption-corrected rest-frame 2–10 keV luminosities ( $L_{2-10 \text{ keV}}$ ) of the 21 X-ray extreme [O III] emitting sources in our sample range from  $1.1 \times 10^{42}$  to  $1.3 \times 10^{45}$  erg s<sup>-1</sup>. Since all the 21 sources have  $L_{2-10 \text{ keV}} > 10^{42}$  erg s<sup>-1</sup>, each is consistent with being an AGN.

The UV slope distribution of the 21 extreme [O III] emitting AGNs at  $z = 1.3$ –3.7 is compared in Fig. 1 (black hatched histogram) to that of the total X-ray AGN sample in the CANDELS fields (grey histogram). Using the parent  $z = 1.3$ –3.7 extreme [O III] emitter sample in T19, we estimate the fraction of extreme [O III] emitting X-ray AGN as a function of UV slope. About 0.3, 0.5, 15, and 26 per cent of the extreme [O III] emitters with UV slopes  $\beta < -2.0$ ,  $= -2.0$  to  $-1.5$ ,  $= -1.5$  to  $-1.0$ , and  $> -1.0$  harbour X-ray AGN, respectively. We note that we do not account for systems such as faint X-ray AGNs or infrared AGNs that the X-ray luminosities may be below the detection limit of current X-ray surveys, so the AGN fractions could be larger. Although extreme [O III] emitting AGNs have relatively red (median  $\beta = -1.0$ ) UV slopes, they are on average bluer than those of the total X-ray AGN sample (median  $\beta = -0.5$ ). As the type II AGN continuum should not contribute significantly at rest-frame UV wavelengths (Assef et al. 2010), it appears that the host galaxies of extreme [O III] emitters are less dusty or more metal-poor than those of the majority of type II AGNs at  $z \sim 1$ –3.

Our goal in this paper is to identify AGNs at intermediate redshifts that are similar to the  $z \simeq 7$ –9 systems thought to harbour AGNs in Laporte et al. (2017) and Mainali et al. (2018). Those objects are characterized by even bluer UV continuum slopes ( $\beta < -2.0$ ; Fig. 1) and very large [O III] + H  $\beta$  EWs ( $> 900$  Å in rest frame) inferred from their extremely red *Spitzer*/IRAC [3.6]–[4.5] colours. Among the 21 sources in our sample, only one object, UDS-24561 (RA = 02:17:44.462, Dec. = -05:11:38.25; Fig. 2), satisfies the joint criteria of  $\beta < -2.0$  and rest-frame  $\text{EW}_{[\text{O III}] + \text{H } \beta} > 900$  Å. By measuring the emission lines shown in the low-resolution ( $R = 130$ ) *HST* grism spectrum (Momcheva et al. 2016; see Section 3.1), the estimated spectroscopic redshift of UDS-24561 is  $z = 3.21$ . We now examine this source in greater detail.

The multiwavelength spectral energy distribution (SED) of UDS-24561 is presented in Fig. 3, which is extracted from the Skelton et al. (2014) photometry catalogues. This object is extremely luminous with absolute UV magnitude  $M_{\text{UV}} = -22.4$ , i.e. about five times brighter than the characteristic  $M_{\text{UV}}^*$  at  $z \sim 3$  ( $M_{\text{UV}}^* \simeq -20.6$ ; see Parsa et al. 2016, and references therein). The UV continuum slope of UDS-24561 is  $\beta = -2.34$  and was computed by fitting a power law ( $f_\lambda \propto \lambda^\beta$ ) to the broad-band fluxes at rest-frame 1250–2600 Å

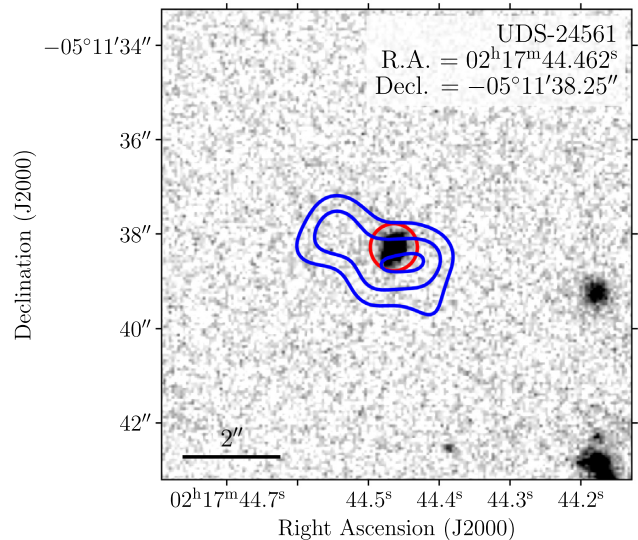


**Figure 2.** Rest-frame UV and X-ray imaging of UDS-24561. The black-white image shows the *HST* F814W (rest-frame UV) postage stamp (10 arcsec  $\times$  10 arcsec) of UDS-24561. The red circle shows the region centred on UDS-24561 with a radius of 0.5 arcsec. The blue contour overlaying the F814W imaging shows the full band (0.5–10 keV) deep *Chandra* X-ray imaging, with contour lines represent count levels of 1, 1.5, and 2. The *Chandra* X-ray source is consistent with the *HST* imaging, indicating that the X-ray emission comes from UDS-24561.

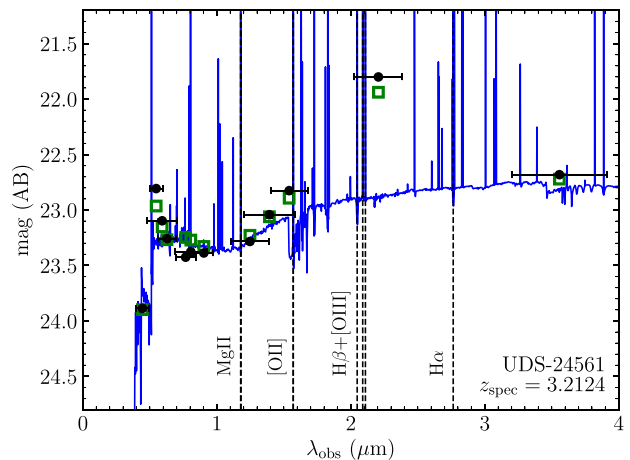


**Figure 3.** The spectral energy distribution of UDS-24561. Observed broad-band photometry extracted from the Skelton et al. (2014) catalogues is shown as solid black circles. The best-fitting SED model inferred from the Bayesian spectral energy distribution modelling and interpreting tool BEAGLE (Chevallard & Charlot 2016) are plotted by solid blue lines, and synthetic photometry is presented by open green squares. The SED of UDS-24561 shows a blue UV slope ( $\beta = -2.34$ ) and an intense *K*-band flux excess indicating a large [O III] + H  $\beta$  EW ( $\simeq 1300$  Å).

(Calzetti, Kinney & Storchi-Bergmann 1994). The intense *K*-band flux excess indicates a large rest-frame [O III] + H  $\beta$  EW ( $\simeq 1300$  Å; see Section 3.1 for more accurate measurements). Both properties are comparable to those of the putative AGN at  $z \simeq 7$ –9 discussed by Laporte et al. (2017) and Mainali et al. (2018). The absorption-corrected  $L_{2-10 \text{ keV}}$  of this object in the Kocevski et al. (2018) catalogue is  $2.75 \times 10^{44}$  erg s<sup>-1</sup>, indicating that it is extremely

luminous. The stellar mass inferred from BEAGLE (Chevallard & Charlot 2016) SED fitting is  $M_* = 2.0 \times 10^{10} M_\odot$ . We note that the current version of the BEAGLE code does not permit including an AGN component, and since we primarily focus on identifying blue, extreme line emitting systems harbouring AGN in this paper, we do not discuss the SED-fitting parameters in detail. We obtained the optical and near-infrared (rest-frame UV and optical) spectra of UDS-24561 via ground-based observations and *HST* archival data. We discuss the spectroscopic observations in the following subsections.

## 2.2 MMT/Binospec spectroscopy

The optical spectrum of UDS-24561 was obtained using the multislit spectrograph Binospec (Fabricant et al. 2019) on the MMT in order to measure the rest-frame UV emission lines. We designed one mask in the CANDELS/UDS field (centred at RA = 02:17:26.8 and Dec. = -05:17:36, with position angle PA = -81°) primarily targeting on UDS-24561. We filled the mask with non-AGN extreme [O III] emitting galaxies at  $z = 1.3-3.7$ , thereby continuing an ongoing survey targeting rest-frame UV metal emission lines (T21a) and the Ly $\alpha$  emission line (T21b) in these systems. We observed this mask between 2020 October and November with a total on-target integration time of 28 800 s during average seeing of 0.9 arcsec. Optical spectra of the targets were taken using the 270 lines mm<sup>-1</sup> grism blazed at 5.5°, with wavelength coverage from 3850 to 9000 Å. The slit width was set to 1.0 arcsec, which results in a spectral resolution of  $R = 1340$ . This mask contains two slit stars to compute the absolute flux calibration, and we also observed spectrophotometric standard stars at a similar airmass in order to correct the instrument response.

The Binospec spectra were reduced using the publicly available data reduction pipeline<sup>1</sup> (Kansky et al. 2019). The pipeline performs flat-fielding, wavelength calibration, sky subtraction, and then the 2D spectra extraction. We created 1D spectra from the reduced 2D spectra using a boxcar extraction, with the extraction aperture matched to the spatial profile of the object. The atmospheric extinction and instrumental response were corrected using the sensitivity curve derived from observations of standard stars. We performed slit loss correction following the similar procedures in T19. We derived the spatial profile of each target from its *HST* F814W postage stamp, and computed the fraction of the light within the slit to that of the total spatial profile. The flux of each spectrum was then divided by the in-slit light fraction measured for each object. Finally, the absolute flux calibration was performed using observations of slit stars, by comparing the slit-loss corrected count rates of slit star spectra with the flux in the Skelton et al. (2014) catalogues.

## 2.3 Keck/MOSFIRE spectroscopy

We also obtained a near-infrared spectrum for UDS-24561 using the Multi-object Spectrometer for Infrared Exploration (MOSFIRE; McLean et al. 2012) on the Keck I telescope. We designed one multislit mask (centred at RA = 02:17:41.25 and Dec. = -05:12:52.26, with position angle PA = 71°) which primarily targets on UDS-24561. The mask was filled with non-AGN extreme [O III] emitting galaxies at  $z = 2.1-3.7$  following the survey strategy discussed in T19. We observed this mask on 2021 March 3 and 4, with a total on-target integration time of 2880 s and an average seeing of 0.8 arcsec. The spectra were taken in the *K* band with wavelength coverage from

1.954 to 2.397  $\mu\text{m}$ , aiming to measure the H $\beta$  and [O III] emission lines for UDS-24561, as well as H $\alpha$  or H $\beta$  and [O III] emission lines for the fillers. The slit width was set to 0.7 arcsec, resulting in a spectral resolution of  $R = 3610$ . We also placed two slit stars on the mask for absolute flux calibration, and observed A0V stars to derive the response spectra and correct for telluric absorption.

The MOSFIRE spectra were reduced using the publicly available PYTHON-based data reduction pipeline<sup>2</sup> (DRP). The pipeline performs flat-fielding, wavelength calibration, and background subtraction before 2D spectra extraction. We created 1D spectra from the reduced 2D spectra using a boxcar extraction. The telluric absorption and instrumental response were corrected using observations of A0V stars. Slit loss correction of each target was performed using the in-slit light fraction computed from its *HST* F160W image. We then performed the absolute flux calibration using observations of slit stars, by comparing the observed fluxes of star spectra with the broad-band photometry.

## 2.4 HST WFC3/G141 spectroscopy

In addition to the MMT/Binospec and the Keck/MOSFIRE *K*-band observations, we use the emission-line measurements in the *HST* Wide Field Camera 3 (WFC3) G141 slitless grism spectrum of UDS-24561 from the 3D-*HST* survey, which is described in detail in Momcheva et al. (2016). The *HST* WFC3/G141 grism has spectral coverage from 1.1 to 1.7  $\mu\text{m}$  (corresponding to ground-based *J* and *H* bands) and a spectral resolution of  $R = 130$ . The grism images were first reduced by removing satellites trails and earthshine, followed by flat-fielding and background subtraction. Then the exposures were combined by interlacing into output mosaic images used for the spectral extractions. After that a contamination model was created to account for overlapping spectra due to neighbouring sources, and the 2D spectra of individual objects were extracted from the interlaced mosaic images and contamination were subtracted. Finally, the 1D spectra were extracted using the optimal extraction procedures (Horne 1986).

## 3 RESULTS

The luminous X-ray detection of UDS-24561 reveals that this system hosts an AGN. In this section, we explore the spectral properties of UDS-24561 in more detail with the optical and near-infrared spectra described in Section 2. We first present the emission line identification and measurements (Section 3.1), then compare the observed line ratios to line diagnostics developed from photoionization models to examine their capability of identifying the nature of the ionizing sources (Section 3.2).

### 3.1 Emission-line measurements

The rest-frame UV and optical spectra of UDS-24561 are shown in Fig. 4. We visually inspect the spectra and identify a number of emission lines including O VI  $\lambda\lambda$ 1032, 1038, Ly $\alpha$ , C IV  $\lambda\lambda$ 1548, 1550, He II  $\lambda$ 1640, Mg II  $\lambda\lambda$ 2976, 2803, [O II]  $\lambda\lambda$ 3727, 3729, [Ne III]  $\lambda$ 3869, H $\beta$ , [O III]  $\lambda$ 4959, [O III]  $\lambda$ 5007, and tentatively Si  $\lambda$ 1393 ( $\sim 2\sigma$ ), while N V  $\lambda\lambda$ 1238, 1243, Si  $\lambda$ 1402, O III]  $\lambda\lambda$ 1661, 1666, and C III]  $\lambda\lambda$ 1907, 1909 emission lines are not detected. The systemic redshift of UDS-24561 is determined using the line centres of non-resonant emission lines with spectral resolution  $R > 1000$ ,

<sup>1</sup>[https://bitbucket.org/chil\\_sai/binospec](https://bitbucket.org/chil_sai/binospec)

<sup>2</sup><https://keck-datareductionpipelines.github.io/MosfireDRP>

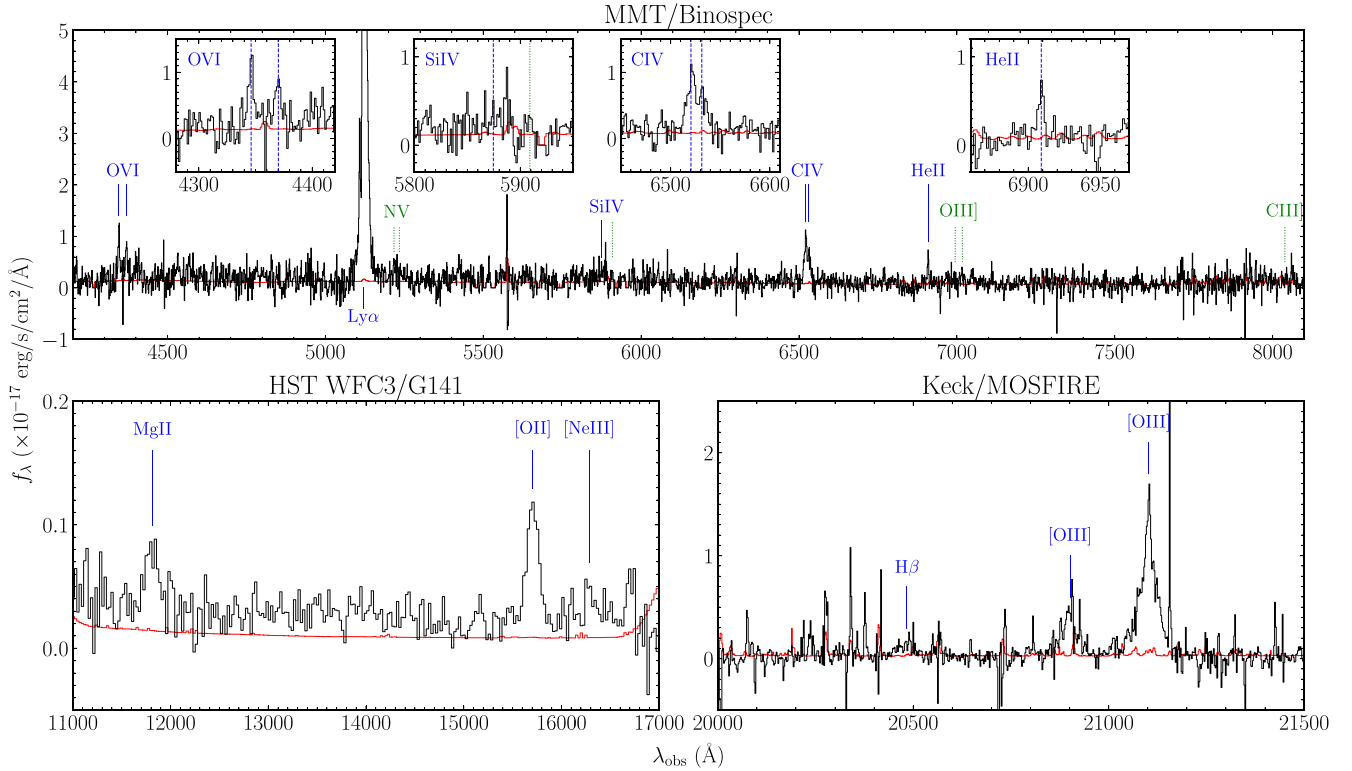


**Figure 4.** Rest-frame UV and optical spectra of UDS-24561. MMT/Binospec, *HST* WFC3/G141, and Keck/MOSFIRE spectra are shown in the top, the bottom left, and the bottom right panel, respectively. The black and red solid histograms represent the observed flux and  $1\sigma$  uncertainty. Detected emission lines including O VI  $\lambda\lambda$ 1032, 1038, Ly $\alpha$ , Si IV  $\lambda$ 1393 (tentatively), C IV  $\lambda\lambda$ 1548, 1550, He II  $\lambda$ 1640, blended Mg II  $\lambda\lambda$ 2976, 2803, blended [O II]  $\lambda\lambda$ 3727, 3729, [Ne III]  $\lambda$ 3869, H  $\beta$ , [O III]  $\lambda$ 4959, and [O III]  $\lambda$ 5007 are marked by blue solid lines. Predicted positions of non-detected N V, Si IV  $\lambda$ 1402, O III, and C III lines are marked by green dotted lines. In the top panel, we also show the zoom-in spectra of O VI, Si IV, C IV, and He II emission lines.

i.e. He II  $\lambda$ 1640, [O III]  $\lambda$ 4959, and [O III]  $\lambda$ 5007 emission lines, resulting in  $z_{\text{sys}} = 3.2124 \pm 0.0006$ .

Emission-line fluxes of UDS-24561 are determined from the extracted 1D spectra. For He II  $\lambda$ 1640, we fit the line profile with a single Gaussian to derive the line flux. For O VI  $\lambda\lambda$ 1032, 1038 and C IV  $\lambda\lambda$ 1548, 1550 doublets, we fit two Gaussians to derive the line flux of each individual component of the doublet. For [O III]  $\lambda$ 5007, we fit two Gaussians with a broad and a narrow component since the emission line cannot be well fitted by a single Gaussian, and the narrow component was used to compute the systemic redshift. The Ly $\alpha$  emission line of UDS-24561 shows a double-peak profile and we fit four Gaussians, so that both blue and red Ly $\alpha$  components can be fitted by broad and a narrow components. For H  $\beta$  and [O III]  $\lambda$ 4959, we calculate the line flux using direct integration instead of fitting Gaussians since these two emission lines are contaminated by sky lines and thus have low signal-to-noise ratio ( $S/N < 4$ ). We also use direct integration to compute the flux of the tentative Si  $\lambda$ 1393 emission line ( $S/N = 2$ ). For the blended Mg II  $\lambda\lambda$ 2976, 2803, [O II]  $\lambda\lambda$ 3727, 3729 doublets and [Ne III]  $\lambda$ 3869 that lie in the *HST* grism spectrum, we use the line flux provided in the Momcheva et al. (2016) catalogues. Previous studies show that the line fluxes measured from *HST* grism spectra are consistent with the values measured from ground-based observations (e.g. Kriek et al. 2015; T19). For the non-detected N V  $\lambda\lambda$ 1238, 1243, Si  $\lambda$ 1402, O III  $\lambda\lambda$ 1661, 1666, and C III  $\lambda\lambda$ 1907, 1909 lines, we derive  $3\sigma$  upper limits by summing the error spectrum in quadrature over  $\sim 200 \text{ km s}^{-1}$ , a value consistent with the upper bound of line widths found for UV metal lines (e.g. Stark et al. 2014).

We next compute the corresponding rest-frame EW for each emission line. Robust measurements of continuum flux are required to compute EWs. For emission lines (except for Ly $\alpha$ ) lying in the MMT/Binospec spectrum that shows bright continuum emission ( $S/N > 5$ ), we derive the continuum flux density in a clean window of  $\pm 150 \text{ \AA}$  near the emission line in the extracted 1D spectrum. For Ly $\alpha$ , we estimate the continuum flux by averaging the flux over rest-frame 1270–1300  $\text{\AA}$  in order to avoid contamination from nearby features (H I absorption blueward of Ly $\alpha$ , and N V, Si II redward of Ly $\alpha$ ; e.g. Matthee et al. 2021). For Mg II, [O II], and [Ne III] in the *HST* grism spectrum, we use the EWs provided in the Momcheva et al. (2016) catalogues. We also compute these EWs by measuring the continuum flux from the grism spectrum and they are in agreement with the EWs provided by the 3D-*HST* team. For H  $\beta$  and [O III] in the Keck/MOSFIRE spectrum where a bright continuum emission is not available, we derive the continuum flux by subtracting the emission line fluxes from the total *K*-band flux. We summarize the emission line measurements of UDS-24561 in Table 1, including the deconvolved full widths at half-maximum (FWHMs) (after subtracting the instrument resolution in quadrature), line fluxes, and EWs.

The most prominent emission line detected in the spectra of UDS-24561 is [O III]  $\lambda$ 5007, with  $\text{EW} = 935 \pm 167 \text{ \AA}$ . The total [O III] + H  $\beta$  EW measured from spectrum is  $1298 \pm 193 \text{ \AA}$ , which is consistent with the value inferred from the *K*-band flux excess ( $\text{EW} \simeq 1300 \text{ \AA}$ ; Fig. 3). Such intense optical line emission is extremely rare at  $z \sim 0\text{--}3$ , but becomes more common in the reionization era (e.g. 20 percent of the  $z \simeq$

**Table 1.** Rest-frame UV and optical emission line measurements of UDS-24561 at  $z = 3.2124$ , including the deconvolved FWHM (column 3), line flux (column 4), and rest-frame EW (column 5). For non-detected N v, O III], and the blended C III] lines,  $3\sigma$  upper limits are provided.

Line	$\lambda_{\text{rest}}$ (Å)	FWHM (km s <sup>-1</sup> )	Flux (10 <sup>-17</sup> erg s <sup>-1</sup> cm <sup>-2</sup> )	EW (Å)
O VI	1031.91	354 ± 54	6.32 ± 1.27	8.6 ± 1.7
...	1037.61	499 ± 99	5.56 ± 1.46	7.6 ± 2.0
Ly $\alpha_{\text{b,n}}$	1215.67 <sup>a</sup>	87 ± 11	13.10 ± 2.17	19 ± 3
Ly $\alpha_{\text{b,b}}$	1215.67 <sup>b</sup>	814 ± 269	11.45 ± 4.20	16 ± 6
Ly $\alpha_{\text{b,t}}$	1215.67 <sup>c</sup>	...	24.55 ± 4.72	35 ± 7
Ly $\alpha_{\text{r,n}}$	1215.67 <sup>d</sup>	513 ± 23	195.8 ± 21.8	280 ± 31
Ly $\alpha_{\text{r,b}}$	1215.67 <sup>e</sup>	987 ± 168	84.07 ± 21.78	120 ± 31
Ly $\alpha_{\text{r,t}}$	1215.67 <sup>f</sup>	...	279.9 ± 30.8	401 ± 44
N v	1238.82	...	<1.46	<2.1
...	1242.80	...	<1.43	<2.0
Si IV	1393.76	...	0.74 ± 0.34	1.1 ± 0.5
...	1402.77	...	<1.43	<2.1
C IV	1548.19	440 ± 65	9.74 ± 1.62	18.2 ± 3.0
...	1550.77	340 ± 83	4.93 ± 1.39	9.2 ± 2.6
He II	1640.42	<216	2.60 ± 0.64	5.3 ± 1.3
O III]	1660.81	...	<1.15	<2.3
...	1666.15	...	<1.07	<2.2
C III]	1908 <sup>g</sup>	...	<3.30	<9.7
Mg II	2798 <sup>h</sup>	...	8.36 ± 1.18	63 ± 10
[O II]	3728 <sup>i</sup>	...	14.94 ± 0.65	172 ± 12
[Ne III]	3870.16	...	3.12 ± 0.70	27 ± 7
H $\beta$	4862.69	...	4.76 ± 2.08	69 ± 30
[O III]	4960.30	...	21.51 ± 6.66	294 ± 91
[O III] <sub>n</sub>	5008.24 <sup>j</sup>	154 ± 21	9.28 ± 1.90	129 ± 26
[O III] <sub>b</sub>	5008.24 <sup>k</sup>	977 ± 131	58.05 ± 11.90	805 ± 165
[O III] <sub>t</sub>	5008.24 <sup>l</sup>	...	67.38 ± 12.05	935 ± 167

Notes. <sup>a</sup>Narrow component of the blue peak of Ly  $\alpha$ .

<sup>b</sup>Broad component of the blue peak of Ly  $\alpha$ .

<sup>c</sup>Total of the blue peak of Ly  $\alpha$ .

<sup>d</sup>Narrow component of the red peak of Ly  $\alpha$ .

<sup>e</sup>Broad component of the red peak of Ly  $\alpha$ .

<sup>f</sup>Total of the red peak of Ly  $\alpha$ .

<sup>g</sup>Total of the blended C III]  $\lambda\lambda$ 1907, 1909.

<sup>h</sup>Total of the blended Mg II  $\lambda\lambda$ 2796, 2803.

<sup>i</sup>Total of the blended [O II]  $\lambda\lambda$ 3727, 3729.

<sup>j</sup>Narrow component of [O III]  $\lambda$ 5007.

<sup>k</sup>Broad component of [O III]  $\lambda$ 5007.

<sup>l</sup>Total of [O III]  $\lambda$ 5007.

7 population has [O III] + H $\beta$  EW >1200 Å; Endsley et al. 2021a).

The [O III] doublets and H $\beta$  emission lines show extended profiles (Fig. 4), and the [O III]  $\lambda$ 5007 line is best fitted by two Gaussians: a narrow component with FWHM = 154 ± 21 km s<sup>-1</sup> and a broad component with FWHM = 977 ± 131 km s<sup>-1</sup> (Fig. 5). A broad line could be due to merger activity, emission from the broad line region of an AGN or AGN-driven outflows. We note that the *HST* image of UDS-24561 (Fig. 2) does not indicate any evidence of merger activity. Moreover, the broad [O III] line width of UDS-24561 is somewhat less than the typical line width seen in AGN broad line regions (FWHM  $\gtrsim$  2000 km s<sup>-1</sup>). Although supernova feedback or shock-ionized outflows can also produce broad line emission, the FWHMs ( $\sim$  300–600 km s<sup>-1</sup>; e.g. Veilleux, Cecil &

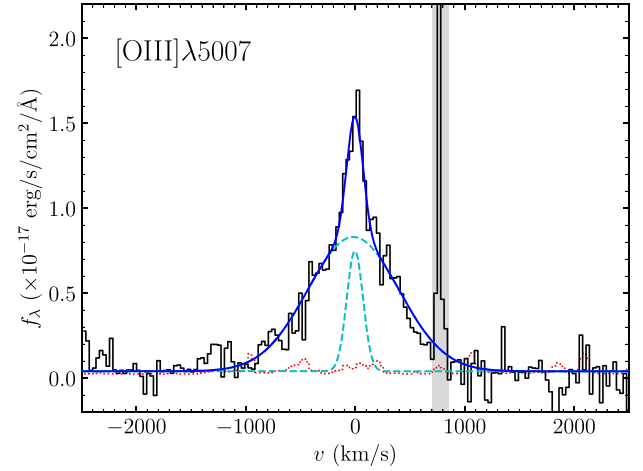


**Figure 5.** Observed [O III]  $\lambda$ 5007 emission line of UDS-24561 and the best-fitting line profile. The  $x$ -axis shows the velocity offset with respect to the systemic redshift. Observed flux and  $1\sigma$  uncertainty are shown by the black solid histogram and the red dotted line. The grey shaded region marks the region that is strongly contaminated by sky line residues. The [O III]  $\lambda$ 5007 emission line is best fitted by a double-Gaussian profile (blue solid line), with a narrow component with FWHM = 154 ± 21 km s<sup>-1</sup> and a broad component with FWHM = 977 ± 131 km s<sup>-1</sup> (both shown by the cyan dashed lines).

Bland-Hawthorn 2005; Freeman et al. 2019; Matthee et al. 2021) are smaller than that of UDS-24561. On the other hand, the broad optical line velocity of UDS-24561 is in agreement with those of AGN outflows (e.g. Förster Schreiber et al. 2014; Genzel et al. 2014; Leung et al. 2017, 2019). We estimate a lower limit to the broad [O III]  $\lambda$ 5007/H $\beta$  ratio using the total flux of H $\beta$  (since we cannot accurately decouple the broad and narrow emission components for H $\beta$ ). The line ratio (>9.3 at  $3\sigma$ ) is consistent with those of AGNs (e.g. Coil et al. 2015; Azadi et al. 2017) and greater than the maximum ratio predicted by starburst models (e.g. Kauffmann et al. 2003; Kewley et al. 2013). Thus, we conclude that the broad optical lines of UDS-24561 likely originate from an AGN-driven outflow.

The Ly  $\alpha$  emission line of UDS-24561 shows a more complex profile (Fig. 6). The emission is double-peaked, and both the blue and red Ly  $\alpha$  components show extended emission line features. None of the blue and red Ly  $\alpha$  component could be fitted by a single Gaussian. However, we find that each Ly  $\alpha$  component is best fitted by two Gaussians including a narrow (FWHM = 87–513 km s<sup>-1</sup>) and a broad (FWHM = 814–987 km s<sup>-1</sup>) component, indicating the blue and red wings extending to maximal velocities of –2000 and +1600 km s<sup>-1</sup> (Fig. 6). The broad wing features, together with the small velocity offset of red peak Ly  $\alpha$  (which is also consistent with the centre of the narrow red Ly  $\alpha$  line) with respect to the systemic redshift ( $\Delta v_{\text{Ly}\alpha} = +141 \pm 76$  km s<sup>-1</sup>), suggest conditions that are conducive to leaking Ly  $\alpha$  photons (e.g. Erb et al. 2014; Hashimoto et al. 2015; Henry et al. 2015; Martin et al. 2015). The total Ly  $\alpha$  luminosity and EW of UDS-24561 are extremely large, with  $L_{\text{Ly}\alpha} = 2.8 \pm 0.3 \times 10^{44}$  erg s<sup>-1</sup> and  $\text{EW}_{\text{Ly}\alpha} = 436 \pm 45$  Å, which the  $L_{\text{Ly}\alpha}$  is  $\sim$ 50 times the typical Ly  $\alpha$  luminosity of LAEs at  $z \sim 3$  ( $L_{\text{Ly}\alpha}^* \simeq 10^{42.7}$  erg s<sup>-1</sup>; e.g. Sobral et al. 2018a). Such luminous  $L_{\text{Ly}\alpha}$  and  $L_{\text{UV}}$  ( $\sim$ 5 times the typical UV luminosity at  $z \sim 3$ ; Parsa et al. 2016), together with the blue UV slope, are consistent with the picture that the physics of accretion discs of massive black holes can destroy the dust in very luminous systems and allow Ly  $\alpha$  and UV photons to escape (e.g. Sobral et al. 2018b).

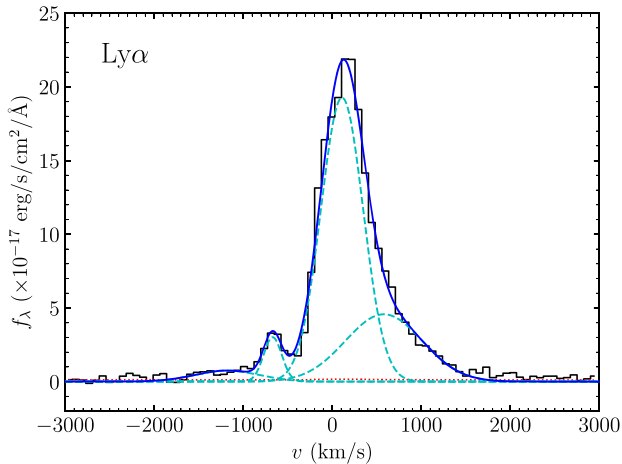


**Figure 6.** Observed Ly $\alpha$  emission line of UDS-24561 and the best-fitting line profile. The  $x$ -axis shows the velocity offset with respect to the systemic redshift. Observed flux and  $1\sigma$  uncertainty are shown by the black solid histogram and the red dotted line. The Ly $\alpha$  emission line shows a double-peaked profile, and each of the blue peak and red peak Ly $\alpha$  line is best fitted by a double-Gaussian profile (a quadruple-Gaussian profile for the total Ly $\alpha$  emission, shown by the blue solid line), with a narrow component (FWHM = 87–513 km s $^{-1}$ ) and a broad component (FWHM = 814–987 km s $^{-1}$ ). Each of the single Gaussian component is shown by the cyan dashed line. The blue (red) wing feature extends to a maximal velocity of  $\sim -2000$  km s $^{-1}$  ( $+1600$  km s $^{-1}$ ).

Intense high ionization emission lines from O VI,<sup>3</sup> Si IV  $\lambda$ 1393, C IV, and He II have also been detected in the rest-frame UV spectrum of UDS-24561 (Fig. 4), suggesting a hard ionizing radiation field powered by an AGN (e.g. Feltre et al. 2016; Volonteri et al. 2017). Unlike Ly $\alpha$ , H $\beta$ , or [O III], we do not detect significant broad emission features for these high ionization lines. As the UV line fluxes are relatively fainter, it could be more difficult to detect broad emission components and deeper spectra are required to measure such features. The line profile of He II is narrow and the line width is comparable to the instrument resolution. We estimate the  $3\sigma$  upper limit of the deconvolved FWHM  $< 216$  km s $^{-1}$  for He II, which is consistent with the FWHM of the narrow [O III]  $\lambda$ 5007 emission line ( $154 \pm 21$  km s $^{-1}$ ). Individual components of the O VI and C IV doublets show wider FWHMs ( $= 340$ – $499$  km s $^{-1}$ ), which could be due to the resonant nature of these emission lines.

The O VI, Si IV  $\lambda$ 1393, C IV, and He II EWs derived from the spectrum of UDS-24561 are  $EW_{\text{OVI}} = 16.2 \pm 2.6$  Å,  $EW_{\text{SiIV}\lambda 1393} = 1.1 \pm 0.5$  Å,  $EW_{\text{CIV}} = 27.4 \pm 4.0$  Å, and  $EW_{\text{HeII}} = 5.3 \pm 1.3$  Å. Significant stellar or interstellar absorption features are not seen in the vicinity of O VI, Si IV  $\lambda$ 1393, or C IV emission lines, although we cannot rule out a modest level of absorption and hence these emission line EWs could be even larger. The majority of metal-poor SFGs do not present such large EWs (e.g. Erb et al. 2010; Vanzella et al. 2016; Senchyna et al. 2017, 2019; Berg et al. 2018, 2019; Du et al. 2020), except a few sources show similar C IV EWs (Stark et al. 2015; Mainali et al. 2017; Vanzella et al. 2017). On the contrary, the high ionization line EWs of UDS-24561 are comparable to the values measured in AGNs (e.g. Hainline et al. 2011; Le Fèvre et al. 2019; Mignoli et al. 2019; Grazian et al. 2020; Saxena et al. 2020). Using the

<sup>3</sup>The spectral resolution of MMT/Binospec allows us to deblend Ly $\beta$  (at rest-frame 1025.73 Å) and O VI  $\lambda$ 1032, 1038 lines.

available UV emission line ratios of UDS-24561, we will test whether the line diagnostics developed to identify ionizing sources are capable of distinguishing between spectra powered by blue, extreme optical line emitting AGNs and massive stars in Section 3.2.

### 3.2 Emission line diagnostics

Various diagnostics involving rest-frame UV emission lines have been developed to determine the nature of the ionizing sources (i.e. star formation, nuclear activity, or shocks) using photoionization models (e.g. Feltre et al. 2016; Nakajima et al. 2018; Hirschmann et al. 2019). The emission line measurements of UDS-24561 provide a unique opportunity to examine the capability of the line diagnostics in identifying AGNs in extreme optical line emitting systems with blue UV slopes. Since blue, extreme [O III] emitting sources are common at  $z > 7$  (e.g. Smit et al. 2015; Endsley et al. 2021a), and UV emission lines will likely remain the most useful diagnostics for studies of the most distant galaxies, our present analysis will provide useful insight into identifying AGNs in the reionization era.

For emission line ratios predicted from photoionization models, we consider the SFG models taken from Gutkin, Charlot & Bruzual (2016) and the latest version of Feltre et al. (2016) AGN narrow-line region models presented in Mignoli et al. (2019). The nebular emission of both models is computed using the photoionization code CLOUDY (Ferland et al. 2013). In this work, we focus on emission line ratios involving O III]  $\lambda$ 1661, 1666 and C IV  $\lambda$ 1548, 1550, He II  $\lambda$ 1640. Since the ionizing spectra of metal-poor hot stars decline rapidly around 50 eV while those of AGNs extend to much higher energies (e.g. fig. 1 in Feltre et al. 2016), the oxygen atoms in AGNs are expected to be largely triply ionized while C IV and He II emission is strong compared to SFGs. We thus expect a decrease in O III] to He II or C IV ratio in AGNs, and these line ratios can be used to determine the ionizing sources.

In the left-hand panel of Fig. 7, we show the C IV/He II versus O III]/He II diagnostic for both nebular emission from photoionization models (magenta squares: AGN; cyan stars: SFG) and observations (red solid symbols: AGN; blue open symbols: SFG). Photoionization models and observations at  $z \simeq 0$ – $4$  in literature indicated that narrow-line AGNs reach smaller C IV/He II ratios ( $< 7$ ) as well as smaller O III]/He II ratios at fixed C IV/He II compared to non-AGN SFGs. The line ratios of the blue, extreme [O III] emitting AGN, UDS-24561, are also consistent with this picture. Using the AGN models in Feltre et al. (2016), we find that the UV line ratios of UDS-24561 are best reproduced by an ionizing spectrum with a slope of  $\alpha \simeq -2.0$  (assuming  $f_\nu \propto \nu^\alpha$  at rest-frame wavelength  $\lambda < 912$  Å) and a very large ionization parameter ( $\log U \simeq -1.0$ ). We also notice that the line ratios of UDS-24561 are located in the AGN–SFG region, implying that they can be reproduced by a few SFG models as well. However, for non-AGN SFG models to reproduce the line ratios of UDS-24561, much lower ionization parameters ( $\log U < -3.0$ ) and larger gas-phase metallicities ( $Z > Z_\odot$ ) are required, both conditions allowing to reduce the emissivity of O III] relative to He II. SFG models with such conditions are not able to reproduce the large C IV EWs seen in AGNs.<sup>4</sup>

<sup>4</sup>Using the BEAGLE tool (Chevallard & Charlot 2016), which adopted the latest version of stellar population synthesis code in Bruzual & Charlot (2003) and the nebular emission models from Gutkin et al. (2016), the largest predicted C IV EW for models with  $\log U < -3.0$  and  $Z > Z_\odot$  is only 1 Å assuming a constant star formation history, which is significantly smaller than the C IV EWs of AGNs.

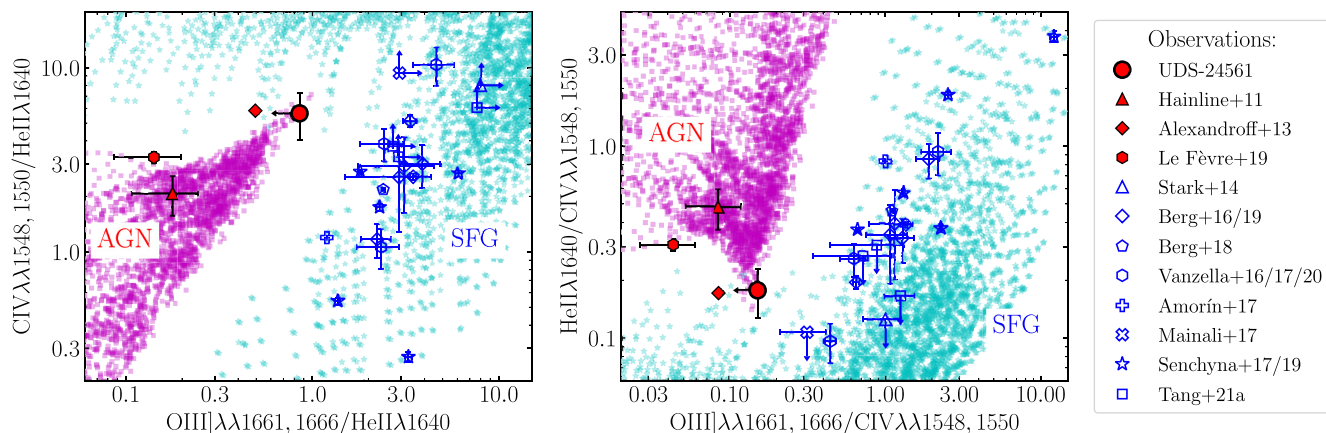


**Figure 7.** *Left:* C IV  $\lambda\lambda 1548, 1550$ /He II  $\lambda 1640$  versus O III]  $\lambda\lambda 1661, 1666$ /He II  $\lambda 1640$  diagnostic diagram (Feltre et al. 2016). *Right:* He II  $\lambda 1640$ /C IV  $\lambda\lambda 1548, 1550$  versus O III]  $\lambda\lambda 1661, 1666$ /C IV  $\lambda\lambda 1548, 1550$  diagnostic diagram (Mainali et al. 2017). Line ratios taken from photoionization models are plotted as magenta squares for AGN models (Feltre et al. 2016; Mignoli et al. 2019) and cyan stars for SFG models (Gutkin et al. 2016). Observed data of UDS-24561 are shown by red circles in both diagnostic diagrams. From the literature, we overlay the data of AGN composite spectra (Hainline et al. 2011; Alexandroff et al. 2013; Le Fèvre et al. 2019; red solid symbols) and SFGs (Stark et al. 2014; Berg et al. 2016, 2018, 2019; Vanzella et al. 2016, 2017, 2020; Amorín et al. 2017; Mainali et al. 2017; Senchyna et al. 2017, 2019, T21a; blue open symbols) at  $z = 0-7$  in both diagrams. Compared to SFGs, AGNs are characterized by smaller O III]/He II and O III]/C IV ratios owing to the hard ionizing spectra that power strong He II and C IV emission and triply ionize oxygen.

The flux ratio of O III] and C IV provides another way to determine the ionizing sources (e.g. Mainali et al. 2017). In the right-hand panel of Fig. 7, we show the He II/C IV versus O III]/C IV diagnostic. The O III]/C IV ratio of UDS-24561 is consistent with those of UV-selected AGNs at similar redshift in literature (Hainline et al. 2011; Alexandroff et al. 2013; Le Fèvre et al. 2019), which are larger than the ratios of non-AGN metal-poor SFGs at fixed He II/C IV ratio. We also notice that the UV-blue AGN UDS-24561 appears to have smaller He II/C IV ratio compared to AGNs with red UV continua at similar redshift in Hainline et al. (2011) and Le Fèvre et al. (2019). This may suggest different properties between these two populations (e.g. metallicity or dust content of the host galaxies, see Section 1). The results presented in Fig. 7 demonstrate that emission line diagnostics involving high ionization lines such as C IV, He II, and O III] are applicable to identifying AGNs in extreme optical line emitting galaxies with blue UV continua. Future spectroscopic observations of a larger statistical sample of such systems will help to confirm the capability of the UV diagnostics in determining the ionizing sources of reionization-era galaxies.

#### 4 DISCUSSION

In the foregoing, we have demonstrated that, from both its detailed spectrum and X-ray luminosity, the extreme line emitting galaxy UDS-24561 contains an AGN. Yet, it is also a close analogue of sources known to be common in the reionization era. UDS-24561 displays a very blue UV slope ( $\beta = -2.34$ ) and a large [O III] + H $\beta$  EW (=1298 Å). Rest-frame optical line emission appears to be prominent at  $z \gtrsim 7$  (e.g. Labbé et al. 2013; De Barros et al. 2019; Endsley et al. 2021a) and 20 per cent of this population has extremely large [O III] + H $\beta$  EW of  $>1200$  Å (Endsley et al. 2021a), similar to the [O III] + H $\beta$  EW of UDS-24561. The UV continuum slopes of the reionization-era population ( $\beta \simeq -2.0$ ) are also bluer than those of star-forming galaxies at lower redshifts (e.g. Bouwens et al. 2012, 2014; Finkelstein et al. 2012). In this section, we consider the implications of UDS-24561 for identifying

AGN activity in reionization-era galaxies and their contribution to the ionizing background at  $z > 6$ .

UDS-24561 provides a detailed glimpse of a population of AGNs that may become common in the reionization era. Its distinct properties relative to more typical AGNs at intermediate redshifts may be useful in locating AGNs at very high redshift ( $z > 6$ ), leading to a better understanding of their role in contributing to cosmic reionization. This is further supported by the fact that extreme optical line emitting systems are likely effective ionizing agents (e.g. Chevillard et al. 2018; Fletcher et al. 2019; T19; T21b).

Unfortunately, identifying AGN activity at  $z \gtrsim 7$  with traditional means is likely to be difficult with current facilities. Current deep X-ray surveys do not have the sensitivity to locate individual examples. Consider, for example, an X-ray source with the same luminosity as UDS-24561. The full (0.5–10 keV), soft (0.5–2 keV), and hard band (2–10 keV) fluxes of UDS-24561 at  $z = 3.2124$  are  $3.01 \times 10^{-15}$ ,  $0.59 \times 10^{-15}$ , and  $2.69 \times 10^{-15}$  erg s $^{-1}$  cm $^{-2}$  (Kocevski et al. 2018), respectively. At  $z = 7$ , such a source would have X-ray fluxes of  $5.84 \times 10^{-16}$ ,  $1.14 \times 10^{-16}$ , and  $5.22 \times 10^{-16}$  erg s $^{-1}$  cm $^{-2}$ , respectively, in the full, soft, and hard bands assuming a power-law index of  $\Gamma = 1.7$  (Brightman et al. 2014). These fluxes are comparable to the  $1\sigma$  sensitivity of the 600 ks deep *Chandra* X-ray survey in the CANDELS/UDS field ( $4.4 \times 10^{-16}$ ,  $1.4 \times 10^{-16}$ , and  $6.5 \times 10^{-16}$  erg s $^{-1}$  cm $^{-2}$  in the full, soft, and hard bands; Kocevski et al. 2018). Although the 4 Ms *Chandra* Deep Field-South survey reaches deeper flux limits (Xue et al. 2011), an individual AGN at  $z = 7$  with  $L_{2-10 \text{ keV}} \lesssim 6 \times 10^{43}$  erg s $^{-1}$  would still be undetected. Not surprisingly, no X-ray counterparts have been seen in all the six luminous ( $L_{\text{UV}} = 1.3-2.5 \times L_{\text{UV}}^*$ ) N V-emitting galaxies at  $z = 6.5-9$  (Tilvi et al. 2016; Hu et al. 2017; Laporte et al. 2017; Mainali et al. 2018; Sobral et al. 2019; Endsley et al. 2021b). Future X-ray facilities will help accumulate larger AGN samples in the reionization era (e.g. Vito et al. 2018).

Likewise the broad H $\beta$  and [O III] emission lines of UDS-24561, which likely reflect AGN-driven outflows, cannot readily be revealed in  $z \gtrsim 7$  spectra with current facilities. Detecting broad emission in individual lines requires relatively high resolution spectra ( $R \gtrsim$

1000) of good quality ( $S/N > 5$ ). Although the blended [O III] + H $\beta$  luminosities and EWs of  $z \sim 7$ –9 systems can be estimated from the *Spitzer*/IRAC [3.6]–[4.5] colours (e.g. Labbé et al. 2013; Smit et al. 2014; De Barros et al. 2019; Endsley et al. 2021a), clearly broad emission cannot be discerned. As with studies of the diagnostic line ratios of [N II]/H $\alpha$  or [S II]/H $\alpha$  in the mid-infrared, rest-frame optical diagnostics of AGN activity at  $z \gtrsim 7$  must await spectroscopy with *JWST*/NIRSpec.

We then consider the feasibility of detecting broad [O III]  $\lambda 5007$  emission in the reionization era with *JWST*/NIRSpec. To robustly measure the broad feature, a good quality ( $S/N > 5$ ) detection of the broad wings is required. If we consider a galaxy at  $z = 7$  harbouring AGN and with broad [O III]  $\lambda 5007$  EW = 800 Å and FWHM = 1000 km s $^{-1}$  (i.e. with parameters similar to those of UDS-24561), the predicted broad [O III]  $\lambda 5007$  emission line fluxes will be  $4.3 \times 10^{-17}$  and  $6.9 \times 10^{-18}$  erg s $^{-1}$  cm $^{-2}$  for a source with the rest-frame optical continuum apparent magnitude of 25 and 27 (–22 and –20 in absolute magnitude; assuming a flat continuum in  $f_\nu$ ), respectively. Using the medium-resolution ( $R = 1000$ ) NIRSpec MSA observations with the G395M/F290LP disperser–filter combination, the *JWST* exposure time calculator predicts the broad wings at  $\pm 1000$  km s $^{-1}$  away from the line centre can be detected with  $S/N = 5$  in 1.5 (continuum magnitude of 25) and 9 h (continuum magnitude of 27). The results demonstrate that reionization-era AGNs can be identified in a relatively short integration time with *JWST*/NIRSpec if they contain broad [O III]  $\lambda 5007$  emission like in UDS-24561.

Signs of AGN activity in the reionization era can also be probed by rest-frame UV spectroscopy. The presence of high-ionization emission lines such as O VI or N V, and strong Mg II line emission suggest hard radiation fields that are likely powered by AGNs. As discussed in Section 3.2 and earlier work (e.g. Alexandroff et al. 2013; Feltre et al. 2016; Laporte et al. 2017; Mainali et al. 2017; Nakajima et al. 2018; Hirschmann et al. 2019; Mignoli et al. 2019), UV line diagnostics are capable of characterizing the shape of the ionizing spectrum and hence distinguishing between AGN and star formation. However, this requires relatively high signal-to-noise ratio spectroscopy that can place key constraints on multiple high ionization UV lines, including C IV and He II.

We have argued in this paper that UDS-24561 may provide a possible template for estimating the abundance of  $z \gtrsim 7$  galaxies hosting AGNs if its combination of intense [O III] emission and blue UV continuum slopes is a key characteristic. Although simply a hypothesis at present given the paucity of examples, the similarity between the properties of UDS-24561 and candidate galaxies with AGN in the reionization era is striking.

Recently, Naidu et al. (2020) interpreted a rapid conclusion of reionization over  $6 < z < 7.5$  in the context of an additional population of rarer, more massive galaxies. In their Model I, bright galaxies with  $M_{UV} < 18$ , which account for less than 5 per cent of the early population, are arranged to account for >50 per cent of the reionizing photon budget. Via this hypothetical model, the rapid evolution in the redshift-dependent neutral fraction  $x_{\text{H I}}$  in the IGM can be matched. Although clearly not a unique interpretation of the  $x_{\text{H I}}$  data, a possible physical explanation of such a mass-dependent contribution of ionizing photons would be the late development of AGNs in a subset of massive galaxies, each of which would have more powerful ionizing capabilities.

As an illustration of this hypothesis in the context of UDS-24561, we can estimate the additional contribution of ionizing photons arising if some proportion of sources with intense [O III] emission and blue UV continuum slopes has a 100 per cent escape fraction due to a powerful AGN. The assumed 100 per cent escape fraction for AGN

is often adopted in studies modelling the contribution of AGN to the ionizing background (e.g. Madau & Haardt 2015). Recent works indicate slightly lower escape fraction for AGNs (e.g. Romano et al. 2019; Iwata et al. 2021; Trebitsch et al. 2021), with an average value of  $f_{\text{esc}} \sim 0.75$  inferred from observations of bright quasars and faint AGNs at  $z \sim 4$  (Cristiani et al. 2016; Grazian et al. 2018). If, for example, 20 per cent of such luminous galaxies harbour AGNs and the escape fraction assigned to this subset is  $f_{\text{esc}} = 1$  ( $f_{\text{esc}} = 0.75$ ), and the remaining sources have  $f_{\text{esc}} = 0.2$ , AGNs can readily supply the required energy budget of 50–60 per cent (40–50 per cent) adopted in Model I in Naidu et al. (2020). Indeed, there is room to relax the adopted escape fraction for non-AGN sources to lower values, depending on the adopted luminosity limit for hosting AGNs.

Although our adopted AGN fraction of 20 per cent in luminous  $z \simeq 6$ –7 is arbitrary, we note that Endsley et al. (2021a) find 20 per cent of  $z \simeq 7$  sources have intense [O III] + H $\beta$  with EW >1200 Å and blue UV continua. Furthermore, although we have adopted a constant ionizing photon production efficiency (i.e. hydrogen ionizing photon production rate per non-ionizing UV luminosity at rest-frame 1500 Å) for all sources regardless of luminosity, a higher value for AGNs would increase their contribution to the ionizing photon budget. These findings illustrate the importance of further examining lower redshift analogues such as UDS-24561.

Given its rarity in the parent sample of extreme [O III] emitters we matched with *Chandra* data, it may be challenging to find further intermediate redshift AGNs similar to UDS-24561. On the other hand, it may be fruitful to focus on extreme [O III] emitters with slightly lower EWs and redder UV slopes given the continuity in the population and the contrast with nearby AGNs in Fig. 1. By expanding such searches to encompass other wide-field surveys, we can hopefully provide the necessary baseline of properties of low-redshift AGNs for comparison with targets in the reionization era.

Ultimately, the statistical baseline of spectroscopic properties of blue, extreme [O III] galaxies harbouring AGNs at intermediate redshift including UDS-24561 will provide useful clues in guiding future *JWST* emission line surveys in the reionization era. Since rest-frame UV and optical spectra of  $z > 6$  galaxies will be obtained by *JWST*/NIRSpec, AGN activities in these systems could be revealed via broad optical emission features or UV line diagnostics involving high-ionization emission lines like C IV and He II as discussed in Section 3. This will provide a valuable census of AGNs at  $z > 6$ , hence constraining the contribution of AGNs to cosmic reionization.

## ACKNOWLEDGEMENTS

MT and RSE acknowledge funding from the European Research Council under the European Union Horizon 2020 research and innovation programme (grant agreement no. 669253). RE acknowledges funding from *JWST*/NIRCam contract to the University of Arizona, NAS5-02015. We would like to thank Nicolas Laporte, Jianwei Lyu, and Feige Wang for useful discussions.

This work is based on observations taken by the 3D-*HST* Treasury programme (GO 12177 and 12328) with the NASA/ESA *HST*, which is operated by the Association of Universities for Research in Astronomy, Inc., under NASA contract NAS5-26555. Part of the observations reported here was obtained at the MMT Observatory, a joint facility of the University of Arizona and the Smithsonian Institution. We acknowledge the MMT queue observers for assisting with MMT/Binospec observations. Part of the data presented herein was obtained at the W. M. Keck Observatory, which is operated as a scientific partnership among the California Institute of Technology, the University of California, and the National Aeronautics and Space

Administration. The Observatory was made possible by the generous financial support of the W. M. Keck Foundation. The scientific results reported in this article are based in part on data obtained from the Chandra Data Archive.

This research made use of ASTROPY, a community-developed core PYTHON package for astronomy (Astropy Collaboration 2013), NUMPY, SCIPY (Jones et al. 2001), and MATPLOTLIB (Hunter 2007).

## DATA AVAILABILITY

The 3D-*HST* data can be accessed from <https://archive.stsci.edu/prepds/3d-hst/>. The data underlying this article will be shared on reasonable request to the corresponding author.

## REFERENCES

- Alexandroff R. et al., 2013, *MNRAS*, 435, 3306
- Allen M. G., Groves B. A., Dopita M. A., Sutherland R. S., Kewley L. J., 2008, *ApJS*, 178, 20
- Amorín R. et al., 2017, *Nat. Astron.*, 1, 0052
- Assef R. J. et al., 2010, *ApJ*, 713, 970
- Astropy Collaboration, 2013, *A&A*, 558, A33
- Azadi M. et al., 2017, *ApJ*, 835, 27
- Barro G. et al., 2019, *ApJS*, 243, 22
- Berg D. A., Skillman E. D., Henry R. B. C., Erb D. K., Carigi L., 2016, *ApJ*, 827, 126
- Berg D. A., Erb D. K., Auger M. W., Pettini M., Brammer G. B., 2018, *ApJ*, 859, 164
- Berg D. A., Erb D. K., Henry R. B. C., Skillman E. D., McQuinn K. B. W., 2019, *ApJ*, 874, 93
- Bouwens R. J. et al., 2012, *ApJ*, 754, 83
- Bouwens R. J. et al., 2014, *ApJ*, 793, 115
- Bouwens R. J. et al., 2015a, *ApJ*, 803, 34
- Bouwens R. J., Illingworth G. D., Oesch P. A., Caruana J., Holwerda B., Smit R., Wilkins S., 2015b, *ApJ*, 811, 140
- Brammer G. B. et al., 2012, *ApJS*, 200, 13
- Brightman M., Nandra K., Salvato M., Hsu L.-T., Aird J., Rangel C., 2014, *MNRAS*, 443, 1999
- Bruzual G., Charlot S., 2003, *MNRAS*, 344, 1000
- Buchner J. et al., 2015, *ApJ*, 802, 89
- Calzetti D., Kinney A. L., Storchi-Bergmann T., 1994, *ApJ*, 429, 582
- Chevallard J., Charlot S., 2016, *MNRAS*, 462, 1415
- Chevallard J. et al., 2018, *MNRAS*, 479, 3264
- Civano F. et al., 2016, *ApJ*, 819, 62
- Coil A. L. et al., 2015, *ApJ*, 801, 35
- Cristiani S., Serrano L. M., Fontanot F., Vanzella E., Monaco P., 2016, *MNRAS*, 462, 2478
- Dayal P., Ferrara A., 2018, *Phys. Rep.*, 780, 1
- De Barros S., Oesch P. A., Labbé I., Stefanon M., González V., Smit R., Bouwens R. J., Illingworth G. D., 2019, *MNRAS*, 489, 2355
- Du X., Shapley A. E., Tang M., Stark D. P., Martin C. L., Mobasher B., Topping M. W., Chevallard J., 2020, *ApJ*, 890, 65
- Endsley R., Stark D. P., Chevallard J., Charlot S., 2021a, *MNRAS*, 500, 5229
- Endsley R., Stark D. P., Charlot S., Chevallard J., Robertson B., Bouwens R. J., Stefanon M., 2021b, *MNRAS*, 502, 6044
- Erb D. K. et al., 2014, *ApJ*, 795, 33
- Erb D. K., Pettini M., Shapley A. E., Steidel C. C., Law D. R., Reddy N. A., 2010, *ApJ*, 719, 1168
- Fabricant D. et al., 2019, *PASP*, 131, 075004
- Fan X. et al., 2006, *AJ*, 132, 117
- Feltre A., Charlot S., Gutkin J., 2016, *MNRAS*, 456, 3354
- Ferland G. J. et al., 2013, *Rev. Mex. Astron. Astrofis.*, 49, 137
- Finkelstein S. L. et al., 2012, *ApJ*, 756, 164
- Finkelstein S. L. et al., 2015, *ApJ*, 810, 71
- Fletcher T. J., Tang M., Robertson B. E., Nakajima K., Ellis R. S., Stark D. P., Inoue A., 2019, *ApJ*, 878, 87
- Förster Schreiber N. M. et al., 2014, *ApJ*, 787, 38
- Freeman W. R. et al., 2019, *ApJ*, 873, 102
- Genzel R. et al., 2014, *ApJ*, 796, 7
- Grazian A. et al., 2018, *A&A*, 613, A44
- Grazian A. et al., 2020, *ApJ*, 897, 94
- Grogin N. A. et al., 2011, *ApJS*, 197, 35
- Gutkin J., Charlot S., Bruzual G., 2016, *MNRAS*, 462, 1757
- Hainline K. N., Shapley A. E., Greene J. E., Steidel C. C., 2011, *ApJ*, 733, 31
- Hainline K. N., Shapley A. E., Greene J. E., Steidel C. C., Reddy N. A., Erb D. K., 2012, *ApJ*, 760, 74
- Hashimoto T. et al., 2015, *ApJ*, 812, 157
- Henry A., Scarlata C., Martin C. L., Erb D., 2015, *ApJ*, 809, 19
- Hirschmann M., Charlot S., Feltre A., Naab T., Somerville R. S., Choi E., 2019, *MNRAS*, 487, 333
- Horne K., 1986, *PASP*, 98, 609
- Hu W. et al., 2017, *ApJ*, 845, L16
- Hunter J. D., 2007, *Comput. Sci. Eng.*, 9, 90
- Iwata I. et al., 2021, *MNRAS*, 509, 1820
- Jaskot A. E., Ravindranath S., 2016, *ApJ*, 833, 136
- Jones E., Oliphant T., Peterson P., 2001, SciPy: Open source scientific tools for Python. Available at: <http://www.scipy.org/>
- Kansky J. et al., 2019, *PASP*, 131, 075005
- Kauffmann G. et al., 2003, *MNRAS*, 346, 1055
- Kewley L. J., Maier C., Yabe K., Ohta K., Akiyama M., Dopita M. A., Yuan T., 2013, *ApJ*, 774, L10
- Kocevski D. D. et al., 2018, *ApJS*, 236, 48
- Koekemoer A. M. et al., 2011, *ApJS*, 197, 36
- Kriek M. et al., 2015, *ApJS*, 218, 15
- Labbé I. et al., 2013, *ApJ*, 777, L19
- Laird E. S. et al., 2009, *ApJS*, 180, 102
- Laporte N., Nakajima K., Ellis R. S., Zitrin A., Stark D. P., Mainali R., Roberts-Borsani G. W., 2017, *ApJ*, 851, 40
- Le Fèvre O. et al., 2019, *A&A*, 625, A51
- Leung G. C. K. et al., 2017, *ApJ*, 849, 48
- Leung G. C. K. et al., 2019, *ApJ*, 886, 11
- Loeb A., Barkana R., 2001, *ARA&A*, 39, 19
- Madau P., Haardt F., 2015, *ApJ*, 813, L8
- Mainali R. et al., 2018, *MNRAS*, 479, 1180
- Mainali R., Kollmeier J. A., Stark D. P., Simcoe R. A., Walth G., Newman A. B., Miller D. R., 2017, *ApJ*, 836, L14
- Marchesi S. et al., 2016, *ApJ*, 817, 34
- Martin C. L., Dijkstra M., Henry A., Soto K. T., Danforth C. W., Wong J., 2015, *ApJ*, 803, 6
- Matthee J. et al., 2021, *MNRAS*, 505, 1382
- McGreer I. D., Mesinger A., D’Odorico V., 2015, *MNRAS*, 447, 499
- McLean I. S. et al., 2012, in McLean I. S., Ramsay S. K., Takami H., eds, Proc. SPIE Conf. Ser. Vol. 8446, Ground-Based and Airborne Instrumentation for Astronomy IV. SPIE, Bellingham, p. 84460J
- Mignoli M. et al., 2019, *A&A*, 626, A9
- Momcheva I. G. et al., 2016, *ApJS*, 225, 27
- Naidu R. P., Tacchella S., Mason C. A., Bose S., Oesch P. A., Conroy C., 2020, *ApJ*, 892, 109
- Nakajima K. et al., 2018, *A&A*, 612, A94
- Nandra K. et al., 2015, *ApJS*, 220, 10
- Oesch P. A., Bouwens R. J., Illingworth G. D., Labbé I., Stefanon M., 2018, *ApJ*, 855, 105
- Oke J. B., Gunn J. E., 1983, *ApJ*, 266, 713
- Onoue M. et al., 2021, *ApJ*, 919, 61
- Ouchi M., Ono Y., Shibuya T., 2020, *ARA&A*, 58, 617
- Parsa S., Dunlop J. S., McLure R. J., Mortlock A., 2016, *MNRAS*, 456, 3194
- Planck Collaboration VI, 2020, *A&A*, 641, A6
- Plat A., Charlot S., Bruzual G., Feltre A., Vidal-García A., Morisset C., Chevallard J., Todt H., 2019, *MNRAS*, 490, 978
- Robertson B. E., Ellis R. S., Furlanetto S. R., Dunlop J. S., 2015, *ApJ*, 802, L19
- Romano M., Grazian A., Giallongo E., Cristiani S., Fontanot F., Boutsias K., Fiore F., Menci N., 2019, *A&A*, 632, A45
- Saxena A. et al., 2020, *A&A*, 636, A47

- Senchyna P. et al., 2017, *MNRAS*, 472, 2608  
Senchyna P., Stark D. P., Chevallard J., Charlot S., Jones T., Vidal-García A., 2019, *MNRAS*, 488, 3492  
Skelton R. E. et al., 2014, *ApJS*, 214, 24  
Smit R. et al., 2014, *ApJ*, 784, 58  
Smit R. et al., 2015, *ApJ*, 801, 122  
Sobral D. et al., 2018b, *MNRAS*, 477, 2817  
Sobral D. et al., 2019, *MNRAS*, 482, 2422  
Sobral D., Santos S., Matthee J., Paulino-Afonso A., Ribeiro B., Calhau J., Khostovan A. A., 2018a, *MNRAS*, 476, 4725  
Stanway E. R., Eldridge J. J., Becker G. D., 2016, *MNRAS*, 456, 485  
Stark D. P. et al., 2014, *MNRAS*, 445, 3200  
Stark D. P. et al., 2015, *MNRAS*, 454, 1393  
Stark D. P., 2016, *ARA&A*, 54, 761  
Steidel C. C. et al., 2014, *ApJ*, 795, 165  
Tang M., Stark D. P., Chevallard J., Charlot S., 2019, *MNRAS*, 489, 2572  
Tang M., Stark D. P., Chevallard J., Charlot S., Endsley R., Congiu E., 2021a, *MNRAS*, 501, 3238  
Tang M., Stark D. P., Chevallard J., Charlot S., Endsley R., Congiu E., 2021b, *MNRAS*, 503, 4105  
Tilvi V. et al., 2016, *ApJ*, 827, L14  
Trebitsch M. et al., 2021, *A&A*, 653, A154  
Vanzella E. et al., 2016, *ApJ*, 821, L27  
Vanzella E. et al., 2017, *ApJ*, 842, 47  
Vanzella E. et al., 2020, *MNRAS*, 491, 1093  
Veilleux S., Cecil G., Bland-Hawthorn J., 2005, *ARA&A*, 43, 769  
Vito F. et al., 2018, *MNRAS*, 473, 2378  
Volonteri M., Reines A. E., Atek H., Stark D. P., Trebitsch M., 2017, *ApJ*, 849, 155  
Xue Y. Q. et al., 2011, *ApJS*, 195, 10  
Xue Y. Q., Luo B., Brandt W. N., Alexander D. M., Bauer F. E., Lehmer B. D., Yang G., 2016, *ApJS*, 224, 15

This paper has been typeset from a  $\text{\TeX}/\text{\LaTeX}$  file prepared by the author.